SDA Visible Range Object Detection Performance Optimization Under Urban Environment

Devin Wu * and Brian C. Gunter †
Georgia Institute of Technology, Atlanta, GA 30363

The ability to track and detect Resident Space Objects (RSO) is essential for maintaining a comprehensive Space Domain Awareness (SDA), especially with the exponential increase in popularity and population of the smaller format satellites. The Georgia Tech Space Object Research Telescope (GT-SORT) maintained by the Daniel Guggenheim School of Aerospace Engineering is one of the unique university-owned raven class telescope facilities dedicated to SDA research tasks. Located on the Georgia Tech campus near downtown Atlanta, the GT-SORT observation site has the advantage of high accessibility for researchers and students alike; however, it suffers from artificial light pollution more so than other traditional observatories. A performance optimization on RSO detection of the facility is therefore critical to extrapolate its full potential. Previous effort has shown that observations of common RSO material, such as gold, white paint, and various types of solar panels, yields the highest limiting magnitude in the near infrared (NIR) and the short wave infrared (SWIR) region [1]. However, the widely used CMOS based camera sensor has a relative quantum efficiency characteristic that drops below 10% at 950nm and above, and the SWIR cameras with mega pixel or higher resolution capability are enlisted under ITAR restricted technology, which restricts the availability of such sensor type data for the general public and for fundamental research purpose. Therefore, spectral optimization within the CMOS camera capability on common RSO surface material types are performed in this study along with collected spectral satellite data to support the optimized model.

Nomenclature

h	=	Planck's constant
c	=	speed of light
r_{sun}	=	radius of the sun
T	=	temperature of the sun

*Graduate Student, Daniel Guggenheim School of Aerospace Engineering
†Associate Professor, Daniel Guggenheim School of Aerospace Engineering, AIAA Senior Member

AU	=	astronomical unit of distance
KB	=	Boltzmann's constant
$QE(\lambda)$	=	spectral quantum efficiency
D_{ap}	=	telescope aperture diameter
P_{pitch}	=	telescope pixel pitch
f	=	telescope focal length
m_{v_0}	=	magnitude zero source
τ_{optics}	=	optic transmittance
τ_{atm}	=	atmospheric transmittance
q_{sky}	=	ambient sky background signature
w	=	angular velocity of the RSO
$m_0(\lambda)$	=	number of pixel occupied by the RSO signature
A_{SO}	=	projected area of the RSO
R	=	distance between the RSO and the observer
q_{SO}	=	energy signal reflected off RSO
α_{SO}	=	wavelength dependent material albedo
τ_{OD}	=	vertical optical depth
V_{hor}	=	horizontal visibility
n_b	=	number of pixel in the sky annulus
N_S	=	sky background per pixel
N_D	=	CCD dark noise per pixel
N_R	=	CCD read noise per pixel
G	=	CCD gain
σ_f	=	digitization lost estimation uncertainty

I. Introduction

Current Residence Space Object detection tasks are typically performed with an "open filter" configuration to maximize the range of wavelength and the total photon flux received[2] or a "V filter" configuration for calibration of the tracking data set against the cataloged star V-magnitude. However, for ground based observation stations located around heavy light polluted locations, such as the Georgia Tech Space Object Research Telescope (GT-SORT) where a typical bright night sky of Atlanta averaging around 16 magnitudes per arcsecond squared for clear nights[3]; thus, a "open" or "V filter" resident space object (RSO) tracking configuration does not provide the best detection performance

in terms of the limiting instrument magnitude. Previous study has shown that optimal band to observe RSO ranges from 780 nm to 2110 nm depending on the sky condition and the type of RSO material to be observed, assuming the observer has access to the most suitable technology that operates under the desired wavebands[1].

Infrared technology has been used in astronomy studies, capturing radiation ranging from 750 to one million nanometers in wavelength, where 0.75 to 5 micrometer range is designated as near-infrared, 5 to 20 micrometer designated as mid-infrared, and wavelengths greater than 20 micrometers considered as far-infrared[4]. The challenges that ground based infrared astronomy faces, however, are usually the presence of water vapor and carbon dioxide in the atmosphere. These two major component of the atmosphere are highly infrared light absorbent, making the atmosphere appeared opaque to many infrared bands; fortunately, there are a few specific wavelength bands between 1 and 5 micrometers at which the atmosphere is partially transparent [4], allowing energy signature to pass through the atmosphere and reach the observer. Infrared observations in the SDA community, especially short-wave infrared (SWIR) ranged observations, has been utilized mainly due to the high infrared reflectance nature of typical satellite materials, such as Gallium arsenide-based solar cells, whose reflectivity at the peak of the V band is around 0.1 while the reflectivity in the K band is around 0.2, nearly twice as reflective as in the V band[5]. Studies of GEO satellites V-K color terms had therefore been conducted with the results indicating a typical 2 to 3 magnitudes difference between the two bands[6].

Although it had been shown that limiting the bandwidth of RSO observation can result in an increased limiting magnitude [1], as the optimal observing bands usually locate in the SWIR range, it is not easy to access a high quality data set in such wavelength region. High resolution infrared observations of RSOs are less accessible due to the ITAR classification of such technology; whereas megapixel CMOS sensors are widely available and are easy to operate for visible wavelength observations. Therefore, in this study, the range of wavelength analyzed is tailored based on the nature of CMOS sensor operating range. Typically, the quantum efficiency (QE) of a CMOS sensor peaks at around 600 to 700 nm, and gradually declines as the wavelength grows[7]. With diminished quantum efficiency in the infrared region, optimal observing band for CMOS based sensor warrants further investigation.

II. Telescope Tracking Environment Modeling

A. Telescope Limiting Magnitudes

A method to derive the wavelength-dependent form of the telescope limiting visual magnitude receiving energy signature from an RSO is developed by Badura[1]:

$$m_{v_{tel}} = 2.5log_{10}\left(\frac{\left(\frac{2\pi hcr_{sun}^2}{\pi(1AU)^2\lambda^5[exp(hc/\lambda K_B T)-1]}\right)\left(\frac{\lambda}{hc}\right)\times 10^{-0.4m_{v_0}}\tau_{optics}\tau_{atm}(\lambda)\left(\frac{\pi D_{ap}^2}{4}\right)QE(\lambda)}{SNR_{lim}\sqrt{2\left(\frac{\sqrt{m_0(\lambda)}\omega}{IFOV}\right)(q_{dark}+q_{sky}(\lambda))}}\right) \tag{1}$$

Where h is Planck's constant, c is the speed of light, r_{sun} represents the radius of the sun, AU stands for an astronomical unit of distance, KB is Boltzmann's constant, $QE(\lambda)$ denotes the spectral quantum efficiency of the focal plane array (FPA) sensor, D_{ap} is the telescope aperture diameter, T is the temperature of the sun, m_{v_0}=26.4 represents the magnitude zero source which is the magnitude of the Vega star[8], τ_{optics} is the transmittance of the optics, τ_{atm} is the transmittance of the atmosphere, q_{sky} is the ambient sky background signature onto the focal-plane, q_{sky} is the dark current of the CCD, and w is the angular velocity of the RSO. IFOV is the instantaneous field of view and is only defined by the telescope geometry pixel-pitch P_{pitch} and focal length f[8]:

$$IFOV = 2arctan\left(\frac{p_{pitch}}{2f}\right) \tag{2}$$

$m_0(\lambda)$ denotes the number of pixel occupied by the RSO signature as a function of the projected area of the RSO perceived by the observer, A_{SO}, and the distance of the RSO, R, and the maximum between the full-width half maximum (FWHM) of atmospheric seeing approximated by the Fried parameter of the system at 500 nm, $r0(500nm)$[9], diffraction, and IFOV:

$$m_0(\lambda) = \left(\frac{A_{SO}}{R\times IFOV} + \frac{1}{IFOV}\times max\left[\begin{array}{c}\frac{\lambda}{r_0(500nm)}\\ \frac{1.22\lambda}{D_{ap}}\\ IFOV\end{array}\right]\right) \tag{3}$$

Maximum achievable SNR is defined as taking the limit of the Poisson process of photon reaching the CCD[10] as integration time goes to infinity[11][12], taking into account of the RSO blurring and sky ambiant signature:

$$SNR_{lim} = \frac{q_{SO}(\lambda)}{\sqrt{2\left(\frac{\sqrt{m_0(\lambda)}\omega}{IFOV}\right)(q_{dark}+q_{sky}(\lambda))}} \tag{4}$$

With q_{SO} denoting the energy signal reflected off a RSO picked up by the focal plane array, assuming the sun is a black body source, and denote the wavelength dependent albedo of the RSO material as α_{SO}:

$$q_{SO}(\lambda) = \tau_{optics}\tau_{atm}(\lambda)\left(\frac{2\pi hc\alpha_{SO}(\lambda)r_{sun}^2}{\pi(1AU)^2\lambda^5[exp^{\left(\frac{hc}{\lambda K_B T}\right)}-1]}\right)\left(\frac{A_{SO}}{R^2}\right)\left(\frac{\pi D_{ap}^2}{4}\right)\left(\frac{\lambda}{hc}\right)QE(\lambda) \tag{5}$$

It can be observed that the limiting magnitudes of telescope systems from Eqn. 1 have three wavelength dependent elements that will effect the spectral optimization result: the background signature of the ambient sky, $q_{sky}(\lambda)[e^-/s/nm]$,

the spectral quantum efficiency of the sensor $QE(\lambda)[e^-/photon]$, and the atmospheric transmittance of the ambient sky $\tau_{atm}(\lambda)[unitless]$. This wavelength dependent function is based on the characteristics of the atmosphere and the sensor noise statistics rather than the properties of the albedo of the object to be detected. For a higher SDA detection performance, it is desired to have $m_{v_{tel}}$ as high as possible so the optical system has a better ability to pick up energy signature even if it's dim.

B. RSO limiting magnitude

The telescope limiting magnitude takes into account the hardware optical characteristics and the atmospheric seeing characteristics at the location of the observer; however, it does not take into account of the spectral reflectance of the RSO material. To consider for the RSO material property in the optimization analysis, modify Eq. 5, which describes the signal picked up by the FPA due to the RSO, to acquire the spectral photon flux originated from the sun, assumed as a black body source, and reflected off RSO in orbit:

$$\phi_{SO}(\lambda) = \left(\frac{2\pi hc\alpha_{SO}(\lambda) r_{sun}^2}{\pi (1AU)^2 \lambda^5 [exp^{\left(\frac{hc}{\lambda K_B T}\right)} - 1]} \right) \left(\frac{A_{SO}}{R^2} \right) \left(\frac{\lambda}{hc} \right) \tag{6}$$

Then, rearrange Eq. 4 to express the RSO signal which traveled through the atmosphere and received by the telescope's photon detector in terms of the defined limiting SNR for detection tasks:

$$q_{SO}(\lambda) = SNR_{lim} \sqrt{2 \left(\frac{\sqrt{m_0(\lambda)}\omega}{IFOV} \right) (q_{dark} + q_{sky}(\lambda))} \tag{7}$$

Expression for the photon flux from an RSO in orbit in terms of the limiting SNR can then be acquired through combining Eq. 5, Eq. 6, and 7:

$$\phi_{SO}(\lambda) = \frac{SNR_{lim} \sqrt{2 \left(\frac{\sqrt{m_0(\lambda)}\omega}{IFOV} \right) (q_{dark} + q_{sky}(\lambda))}}{\tau_{optics} \tau_{atm}(\lambda) \left(\frac{\pi D_{ap}^2}{4} \right) QE(\lambda)} \tag{8}$$

We also need to define the photon flux from the magnitude zero space object, Vega, to calculate the visual magnitude of the space object:

$$\phi_0(\lambda) = \left(\frac{2\pi hc\alpha_{SO}(\lambda) r_{sun}^2}{\pi (1AU)^2 \lambda^5 [exp^{\left(\frac{hc}{\lambda K_B T}\right)} - 1]} \right) \left(\frac{\lambda}{hc} \right) \times 10^{-0.4 m_{v_0}} \tag{9}$$

The visual magnitude of the RSO can then be scaled through the expression which compare the photon flux reflected off of the RSO to the reference point zero magnitude object photon flux[13]:

$$m_{v_{SO}} = 2.5log_{10}\left(\frac{\phi_0(\lambda)}{\phi_{SO}(\lambda)}\right) \tag{10}$$

Combining Eq. 6, Eq. 9, and Eq. 10, it can be shown that the wavelength dependent apparent visual magnitude of the RSO is only affected by the reflectance propertie of the material:

$$m_{v_{SO}} = 2.5log_{10}\left(\frac{\pi \times 10^{-4m_{v_0}}}{\alpha_{SO}(\lambda)\left(\frac{A_{SO}}{R^2}\right)}\right) \tag{11}$$

The above equation gives us the part of the objective function that take into account the material property of the RSO with respect to the wavelength spectrum; combine this with the telescope limiting magnitude of Eq. 1, we can proceed to construct the objective function for this optimization study.

C. Spectral optimization objective function

With the expression of telescope limiting magnitude and the RSO magnitude described by Eq. 1 and Eq. 11, we can create a objective function that will allow the optimization of a telescope system's RSO detectability be conducted with respect of observing wavelength characteristics. Taking a closer look into the nature of $m_{v_{tel}}$, it is the limit of the telescope optic system's ability to pick up any meaningful energy signal within its field of view, and differentiate the signal apart from the general background noise. The ideal system would be able to detect signal as weak as possible, therefore, in the context of visual magnitude system, it is desirable to achieve a $m_{v_{tel}}$ as high as possible, since the magnitude system operates in a higher signal lower value fashion. On the other hand, $m_{v_{SO}}$ represents the energy originated from the sun and then bounced off the RSO object to be detected in terms of visual magnitudes; therefore, the brighter the $m_{v_{SO}}$, the better chance the optic system has to pick up its signal from the background noise; in other words, it is desirable to have a lower $m_{v_{SO}}$ value. Hence, the objective function should seek to minimize $m_{v_{SO}}$ and maximize $m_{v_{tel}}$ simultaneously:

$$f_{obj}(\lambda) = -1 \times m_{v_{SO}} + m_{v_{tel}} \tag{12}$$

Normalization of the two objective parts were performed in order to ensure equal weighting between the two[14]. Also, to re-frame a minimization problem from a maximization one, a constant of -1 is applied to Eq. 12:

$$f_{obj}(\lambda) = -1 \times [norm(-1 \times m_{v_{SO}}) + norm(m_{v_{tel}})] \tag{13}$$

Where the normalization process of the i^{th} visual magnitude function can be express as follow:

$$norm(m_i(\lambda)) = \frac{m_i(\lambda) - m_{i_{min}}}{m_{i_{max}} - m_{i_{min}}} \tag{14}$$

In this study, the particular interest in the CMOS based sensor bounds the range of optimization from 350nm to 900nm, and a typical $QE(\lambda)$ curve is shown in Fig. 1. For longer wavelength observations, an infrared InGaAs (1000nm to 1500nm $QE(\lambda)$ capability) or a far-infrared InGaAs (1500nm to 2500nm $QE(\lambda)$ capability[15]) type sensor is needed; however, commercially available short-wave infrared sensor (SWIR) provides only sub-megapixel resolution quality, and the megapixel counterparts are International Traffic in Arms Regulations (ITAR) restricted, limiting the availability of such sensors to the general public. The value of $QE(\lambda)$ used is the maximum of the three color channel at a given wavelength, for example, the B channel $QE(\lambda)$ value will be selected at λ = 465nm instead of the G channel value. This method models the current hypothetical capability of the GT-SORT under a constant atmospheric condition.

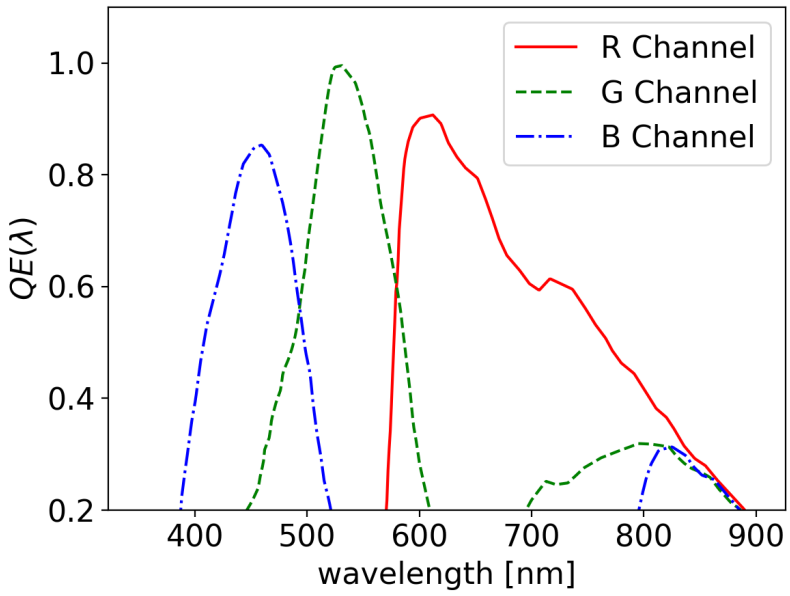

Fig. 1 Typical quantum efficiency curve of a multi-channel CCD (adapted from [16])

For the RSO material of this study, four common satellite surface material are considered: indium gallium arsenide (InGaAs) solar panels, Gallium indium phosphide ($GaInP_2$) solar panels, gold, and white paint. The RSO is assumed to have constant material reflectance across the nadir pointing facet. Reflectance characteristic studies of gold, white paint, and InGaAs were performed by Reyes and Cone[17], and the $GaInP_2$ material characteristics were adapted from[18]; as shown in Fig. 2.

The MODerate resolution atmospheric TRANsmission program (MODTRAN) with added city light pollution considerations was used by Badura for atmospheric modeling[1] and is also used here since the simulation scenario are both according to the condition of Atlanta, where GT-SORT locates. Although MODTRAN is most prominent in

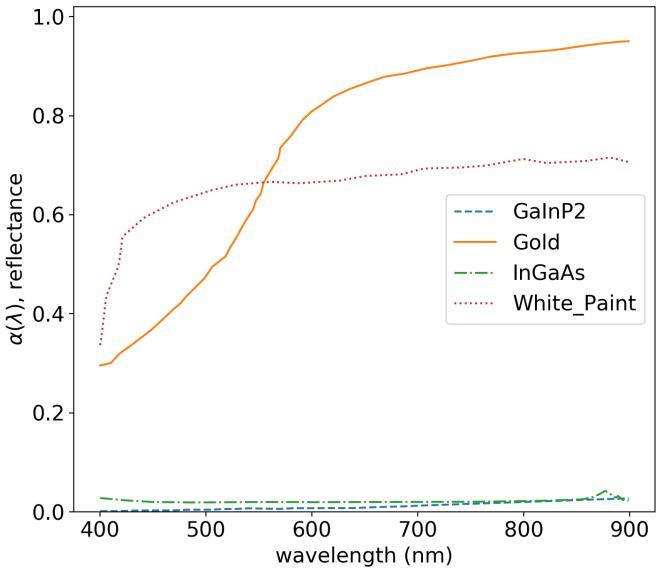

Fig. 2 Material reflectance derived from[17]

the remote sensing community for its capability of modeling the atmosphere up to an altitude of 100 km above mean sea-level with 30 discrete layers of different atmospheric layer properties[19], it is also able to perform sky background spectra considering Atlanta's geological location and the downward transmittance modeling for this study.

We assume a 90° lunar phase angel for a half-moon observing condition. Also, a moderately hazy sky condition is used for this study which is defined by a vertical optical depth ('τ_{OD}') of 0.473 km and a horizontal visibility (V_{hor}) of 8.879km. A typical clear sky would have 0.254 km of 'τ_{OD}' and 25.246 km of V_{hor}, and a hazy sky would have 0.623 km of 'τ_{OD}' and only 5.386 km of V_{hor} seeing[20][21]. The light pollution source type percentage contribution is modeled after Los Angeles[22] in Table 1. The resultant atmospheric transmittance and the spectral radiance are presented in Fig. 3 and Fig 4. Under the same telescope tracking environment parameters, the telescope limiting magnitude objective function can also be calculated, as shown in Fig. 5.

Light source type	Contribution to city light (%)
High Pressure Sodium	55
Metal Halide	20
Mercury Vapor	10
Incandescent	10
Low Pressure Sodium	5

Table 1 Contribution of light source type to the overall city brightness[22].

Optical parameters of GT-SORT defined by Coder[11] were adapted to create an accurate optical model representation

for our scenario. Optical along with other properties used to simulate the GT-SORT tracking environment are shown in Table 2.

Parameter	Symbol	Value	Unit
Limiting SNR	SNR_{lim}	4	-
Fried Parameter at 500 nm	$r_0(500nm)$	0.025	m
Dark Current	q_{dark}	2	$[e^-/s/nm]$
Optical Transmittance	τ_{optics}	1.0	-
Pixel Pitch	p_{pitch}	5.4	μm
Focal length	f	3	m
F-number	$f\sharp$	6	-
Aperture Diameter	D_{ap}	1	m
Zenith Angle	θ	0	degrees
Astronomical Unit (AU)	AU	$1.496e^{11}$	m
Projected Area of Space Object	A_{SO}	1	m^2
RSO Angular Velocity	ω	$7.27e^{-5}$	rad/sec
Lumens per Capita	L	2500	lumens/person

Table 2 GT-SORT telescope tracking environment properties

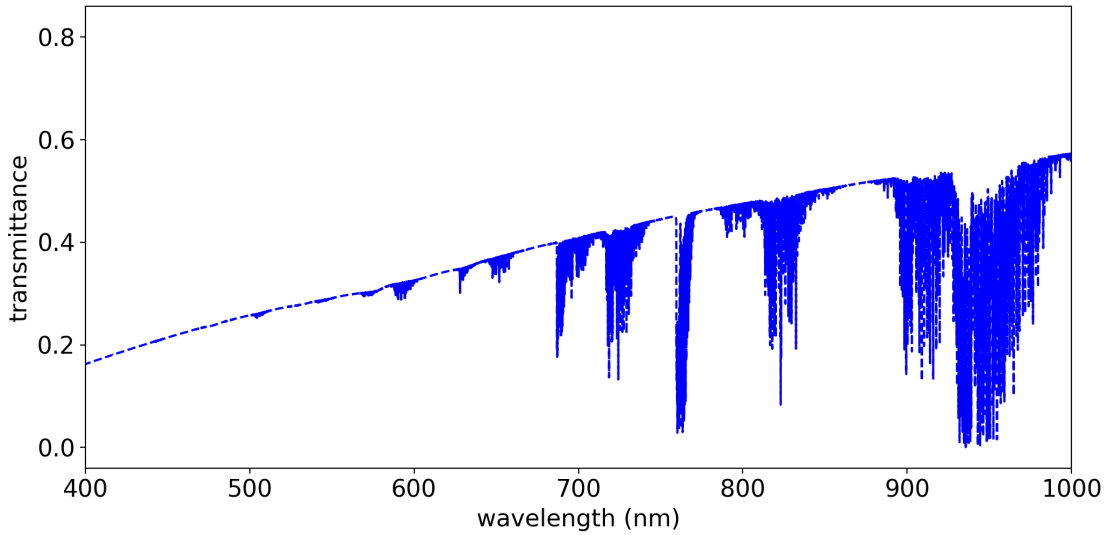

Fig. 3 Transmittance of a moderately hazy Atlanta sky background

III. Optimization Result

Optimization results are generated using Eq. 13 from a minimal bandwidth matching up to the Johnson Cousin's filter set, the filter transmittance graph is shown in Fig. 6[8], and up to 500 nm where the transmittance curve covers the entire CCD operating range, simulating an open filter detection environment. Convolution of a rectangular band-pass with the derived objective function Eq. 13 was performed to carry out the minimization problem for each of the

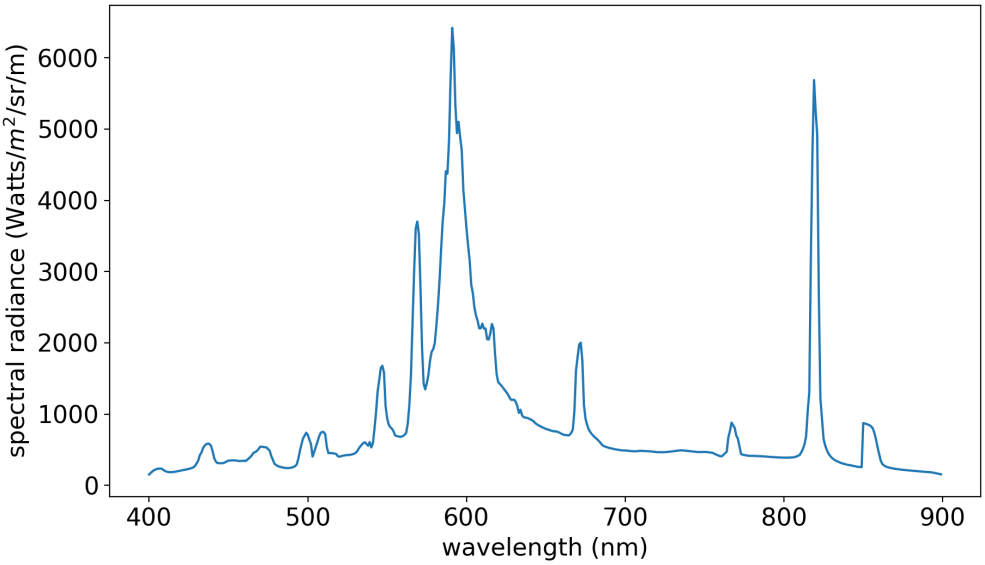

Fig. 4 Spectral radiance picked up by the telescope aperture due to the polluted sky background

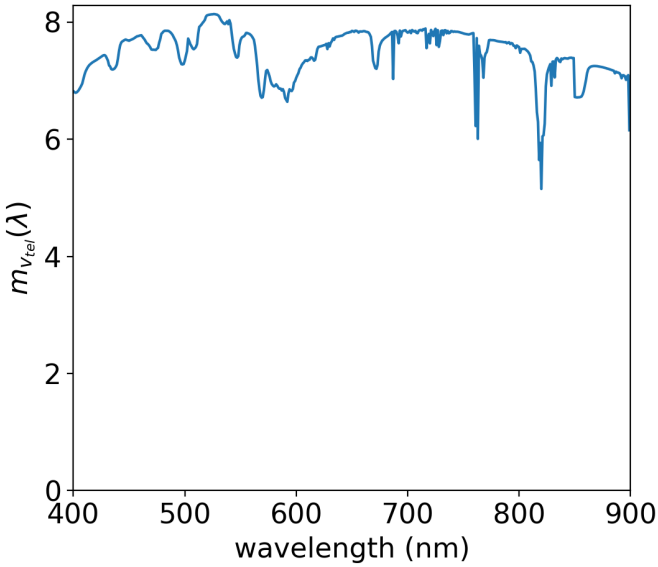

Fig. 5 GT-SORT limiting magnitude

interested material type, where the minimal value resulting from this series of operations was then considered to be the optimal band-pass center wavelength for the given bandwidth and the detection of the given material type. Tracking environment is assumed to have a half-moon illumination condition with moderate aerosol value representing a mid-level hazy atmosphere. The resultant objective function $f_{obj}(\lambda)$ fluctuates along the wavelength λ and is unique to each material type. $f_{obj}(\lambda)$ for each of the four materials are shown in Fig. 7, and the final optimal band center for each

bandwidth is tabulated in Table. 3.

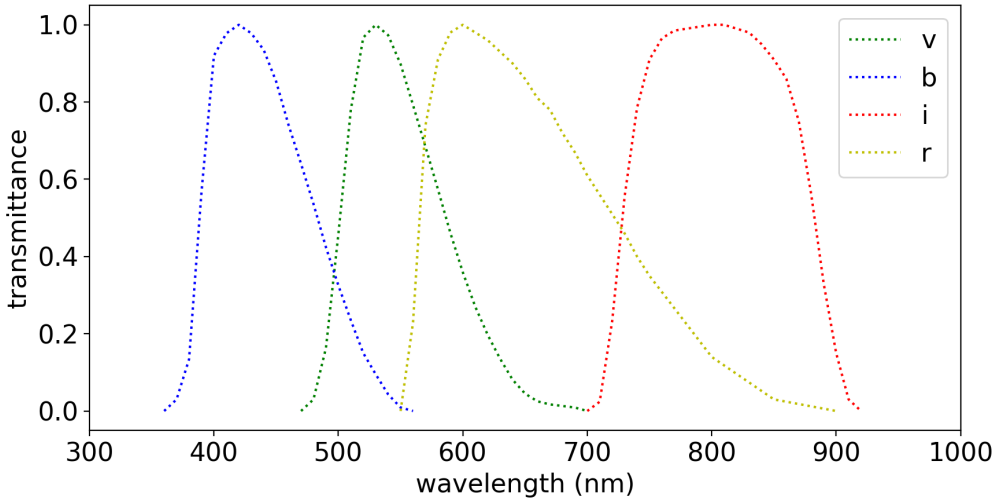

Fig. 6 Johnson Cousin's filter transmittance curve[8]

The results show an apparent trend that an open filter tracking environment does not provide the optimal detection capability from the telescope system; however, there is no one single definite optimal detection band for RSO observations, as it is dependent on the material type specific to the tracking task. For an InGaAs solar panel detection task with applied Johnson Cousin-like narrow band-pass filter with 100 nm bandwidth, the optimal band center is located at 843 nm, which does not correlate to the 761 nm of the optimal band center for a 100 nm band-pass $GaInP_2$ solar panel detection task. It can also be noted that the optimal narrow band-pass band center for InGaAs solar panel detection matches well with the I_r band filter characteristic from the Johnson Cousin's filter set, the rest of the material type detection task result in an optimal narrow band detection center between the R_c and the I_r filter bands. We can also find the relative expected performance between the Johnson Cousin's filters on detecting a specific material type by comparing the corresponding objective function value under the filter wavelength range. For a $GaInP_2$ solar panel detection task with Johnson Cousin's filter set, the I_r filter is expected to produce the highest SNR, followed by the R_c filter, then the V filter, and finally the B filter.

IV. Collected Satellite Observation Data

Images of the GOES 16 geostationary weather satellite were collected during the night of April 16^{th} with applied Johnson Cousin's filter set. The collection run started at 01:22 Coordinated Universal Time (UTC) with two operators on deck and one joined remotely. GOES 16 is the first in the GOES-R series system of the Geostationary Operational Environmental Satellite, with mission requirements established by the National Weather Service (NWS), National Environmental Satellite, Data, and Information Service (NESDIS), and the National Oceanic and Atmospheric

InGaAs Solar Panel		
Bandwidth (nm)	Band center (nm)	$f_{obj}\lambda$
100	843	-0.5336
150	819	-0.5119
200	794	-0.5054
250	769	-0.4963
300	749	-0.4835
350	724	-0.4657
400	699	-0.4656
450	669	-0.4621
500	650	-0.4640

(a) Optimal InGaAs detection bands

White Paint		
Bandwidth (nm)	Band center (nm)	$f_{obj}\lambda$
100	710	-0.9129
150	720	-0.9060
200	714	-0.8993
250	725	-0.8798
300	662	-0.8778
350	639	-0.8720
400	650	-0.8639
450	674	-0.8589
500	650	-0.8381

(b) Optimal white paint detection bands

$GaInP_2$ Solar Panel		
Bandwidth (nm)	Band center (nm)	$f_{obj}\lambda$
100	761	-0.8399
150	775	-0.8225
200	796	-0.8200
250	774	-0.8100
300	750	-0.7901
350	724	-0.7632
400	700	-0.7550
450	675	-0.7358
500	650	-0.7050

(c) Optimal $GaInP_2$ detection bands

Gold		
Bandwidth (nm)	Band center (nm)	$f_{obj}\lambda$
100	710	-0.9113
150	720	-0.9039
200	715	-0.8963
250	745	-0.8764
300	749	-0.8672
350	724	-0.8467
400	700	-0.8300
450	675	-0.8012
500	650	-0.7615

(d) Optimal Gold detection bands

Table 3 Optimal detection bands for InGaAs solar panel, $GaInP_2$ solar panel, white paint and gild

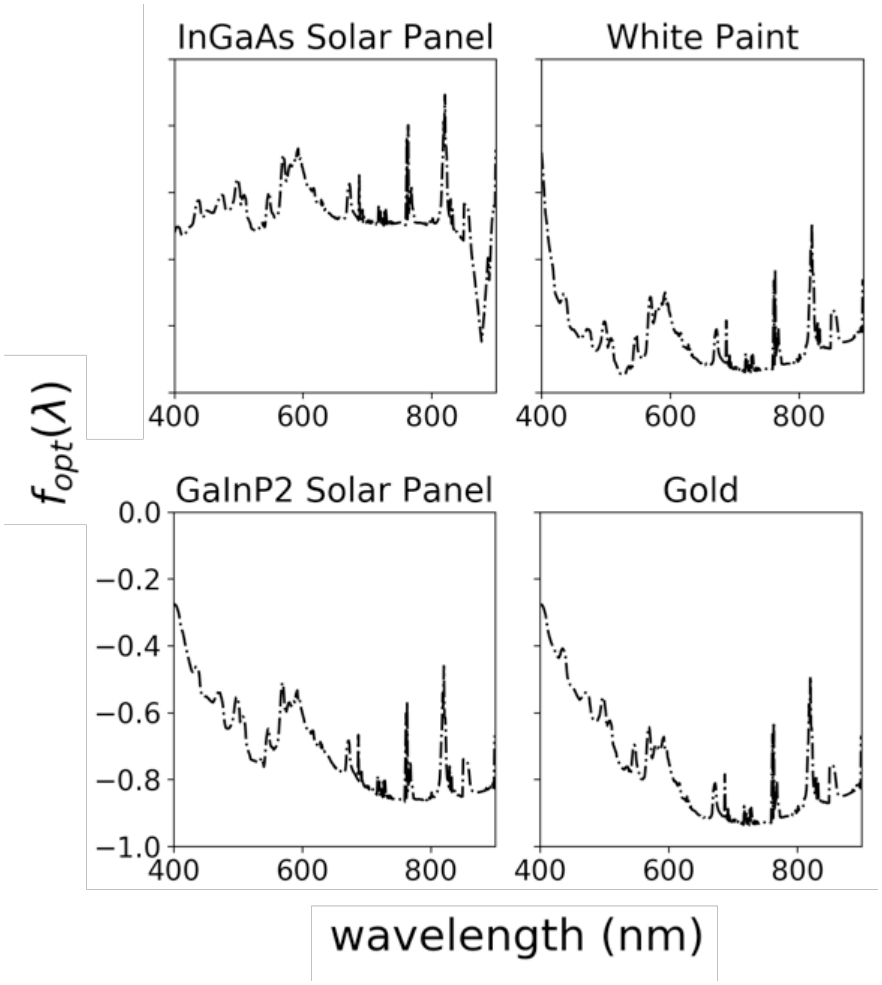

Fig. 7 Objective function output for the materials

Administration (NOAA) to provides life-saving observations of high-impact environmental phenomena such as severe storms, hurricanes, fires, and volcanic eruptions, monitor the Earth's surface and space environmental conditions to provide warning for space weather effects on orbiting satellites, communications systems, the electric grid, aviation workers and passengers, and introduce improved atmospheric and oceanic observations and data dissemination capabilities[23].

The majority of the GOES 16's surface area is contributed by the solar array assembly, shown in Fig. 8, which comprise of 6720 ultra-triple junction (UTJ) photovoltaic cells supplied by Spectrolab[24]. Each solar panel has a dimension spanning across 135.7 cm × 392.3 cm, and there are five panels in total for the complete solar array assembly. The solar array is expected to produce 4960 W at summer solstice and 5600 W at vernal equinox at the end of the 15 year mission.

In order to support the optimization result, it is important to understand the material property of the UTJ photovoltaic cell. This type of triple-layered solar cell comprises of a monolithic, two terminal triple junction ($III - V$) structure[25].

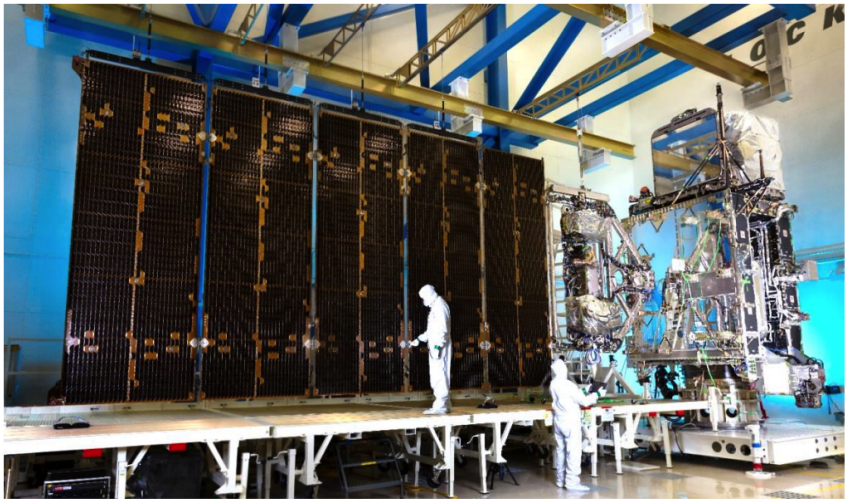

Fig. 8 GOES 16 solar array installation[24]

At the top most layer is the $GaInP_2$ solar cell, followed by the GaAs solar cell in the middle layer, and a Germanium bottom cell with a Germanium substrate; the layers are interconnected with two tunnel junctions, illustrated in Fig. 10.

Fig. 9 Spectrolab 28.3% Ultra Triple Junction solar cell (left) and the cell structure (right)[25]

It can be observed that the $GaInP_2$ solar cell is positioned so that it is directly exposed to and reflecting the incoming solar photon energy flux; therefore, the objective function curve of the $GaInP_2$ solar cell from Fig. 7 is used here to compare with the collected data.

A. Data reduction

The GEOS 16 data sets was collected with a 5-second exposure time and 450 gain from the CCD for all applied filters; the configuration was then used as a baseline for bias, dark, and flat data sets [26]. Bias frames serve as a noise

characterization resulting from the camera electronics, and theoretically the frames should be collected through a closed shutter zero-length exposure time and the same gain as the RSO detection set configuration. However, the CCD does not allow zero-length exposures; therefore, the minimum possible exposure time was used, which in our case is 32 microseconds. A master bias frame was then created by taking the average of the bias frames.

Randomly generated electrons due to the atoms in the material bumping into one another, characterized as the thermal noise, create noise within the CCD chip. To reduce this effect, active CCD cooling was engaged during data collection with a temperature set point designated at 0 degree Celsius. Dark frames of the CCD with the same observing configuration as the GEOS 16 data sets were also collected to reduce the thermal noise from the satellite observation. The bias and the dark frames were both captured in a low to none light source environment with the CCD sensor capped to prevent external photon leakage. A master dark frame was then created by taking the average of the dark frames.

Optical path of a telescope system can obscure incoming Lambertian signature with dust on the mirrors, camera window, and/or filters as well as vignetting. Similar effect can also be contributed from the CCD sensor itself, since the pixel sensitivity normally does not hold constant across the sensor field of view. In order to remove this hardware characteristic from the observation data, flat frames are collected with the aforementioned CCD observing gain configuration, and an exposure time that allows the average pixel value at around 60% without saturating any of the pixels. The collection run started as the sky got dark enough to avoid saturating the chip and ended before any star appeared in the frame. Telescope was positioned for a near-zenith pointing during the run. Similar to the other two data primer sets, a master flat frame was created by taking the average of the flat frames. The observation set can then be reduced with the master bias frame, the master dark frame, and the master flat frame to represent data from the target, stars, and sky background, as shown in Fig. 10 .

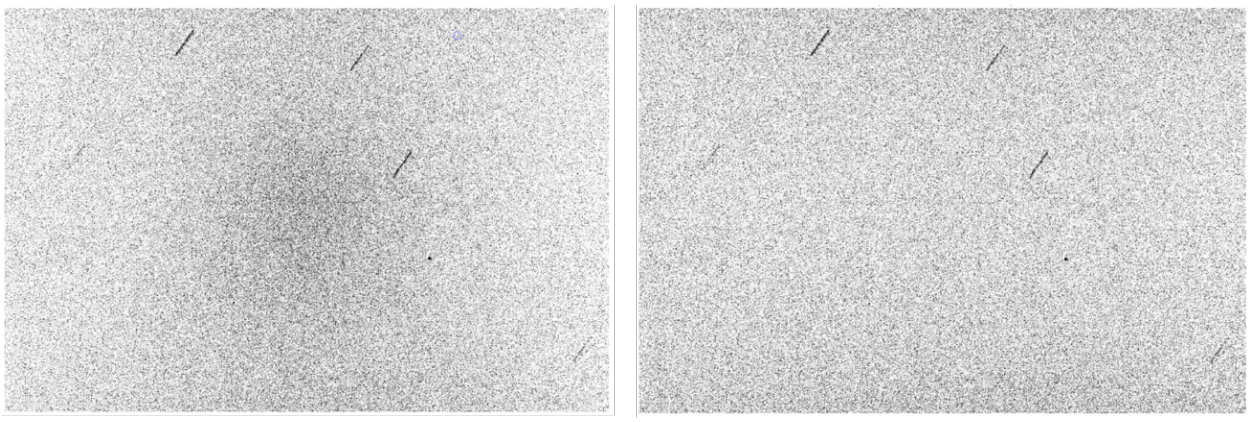

Fig. 10 Negative of the raw image of GOES 16 gathered during the night of April 16^{th} (left) and the same image reduced by bias, dark and flat (right); the brightness and contrast of the images have been adjusted for better visual presentation. The elongated signatures were stars streaking through the background, and the dot signature is the satellite itself.

The energy signature SNR from the satellite was extracted using the photometry aperture and annulus method[26].

An aperture isolates the area considered as the target signature. The diameter of the aperture is most commonly set around 3 times the FWHM of the target energy distribution. An annulus set around the measuring aperture defines the local background area near the target charactrized by its inner radius and outer radius. Size of the sky annulus can vary as long as the inner radius is set after the target's normalized energy profile reaches zero. Once an aperture annulus set is defined, the same configuration should be applied throughout the data set. Aperture annulus source extraction configuration for the GOES 16 data set is shown in Fig. .

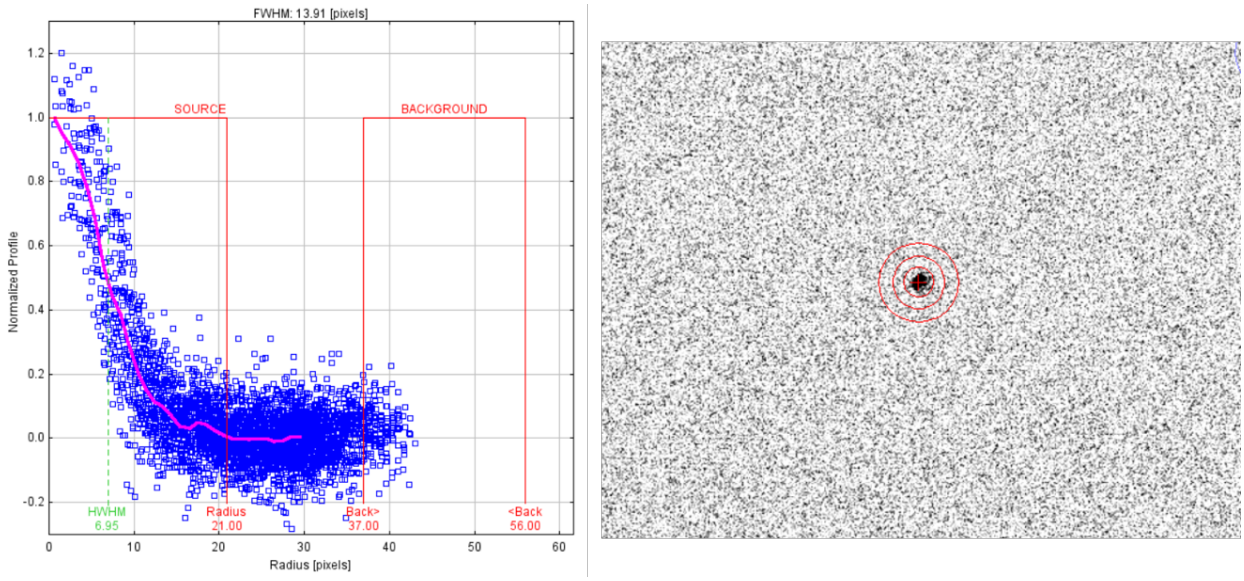

Fig. 11 GOES 16 data set target source extraction aperture and annulus (right) and radial normalized profile (left).

The target source value is calculated by integrating all pixel value whose center falls within the measuring aperture with each pixel reduced by the sky background value, where the sky background value is defined by the average pixel value within the sky annulus. CCD noise taking into account of the contributions from read-out-noise, dark current, and target source and sky Poisson noise was modeled by Merline and Howell in the "CCD equation"[27], shown in Eq. 15.

$$Noise_{CCD} = \sqrt{N_{sig} + n_{pic}\left(1 + \frac{n_{pix}}{n_b}\right)\left(N_s + N_D + N_R^2 + G^2\sigma_f^2\right)} \tag{15}$$

Where n_{pic} is the number of pixel occupied by the target, n_b is the number of pixel in the sky annulus, N_S is the sky background per pixel, N_D is the CCD dark noise per pixel, N_R is the CCD read noise per pixel, G is the CCD gain, and σ_f is the uncertainty in estimating the true mean of the fractional count lost to digitization per pixel with value is estimated at 0.289ADU (accessory dwelling unit).

Dividing the target source, N_{sig} value by the CCD noise, the SNR for RSO detection can be calculated as shown in Eq. 16

$$S/N = \frac{N_{sig}}{\sqrt{N_{sig} + n_{pic}\left(1 + \frac{n_{pix}}{n_b}\right)\left(N_s + N_D + N_R^2 + G^2\sigma_f^2\right)}} \tag{16}$$

With Eq. 16, the SNR of GOES 16 is extracted along with the target source energy level in terms of pixel value and is used to compare against the result generated with the RSO detection objective function, Eq. 13, in the case of a $GaInP_2$ solar panel.

B. Observation results

We first generate the average value of the $GaInP_2$ solar panel detection objective function under the operating range of the B, V, Rc, Ir Johnson Cousin's filters, tabulated in Table 4.

Johnson Cousin's filter band	$GaInP_2$ detection objective function value
B	-0.5075
V	-0.6364
Rc	-0.7253
Ir	-0.7350

Table 4 Average $GaInP_2$ solar panel detection objective function value under Johnson Cousin's filter bands.

From the table above, we can determine that Ir filtered data will yield the highest target SNR since it has the most negative objective function value and we are treating the analysis as a minimization problem. Closely following that is the Rc band, then the V band, and finally the B band. Note that the simulated optimal detecting band from the analysis is centered at 761 nm, which is between the band center of the Rc band and the Ir band, with an objective function value of -8.399, as shown in Table 3.

The total pixel value of GOES 16 is shown in Fig. 12. It can be observed that the Ir band received the most optical energy flux from GOES 16 and the B band received the least amount, which corresponds to the higher material reluctance property of its solar array closer to the 900 nm wavelength region and the lower reflectance at around 400 nm. As for the V band energy flux, the higher peaking CCD QE curve in this wavelength region allowed it to receive more incoming photon than that of the Rc band data, even though the material has a slightly higher reflectance in the Rc band than the V band. However, the above observation does not directly correlate to the detectability of the filters, we need to look at the target SNR to determine the object detectability. The GEOS 16 data SNR, calculated using Eq. 16 is shown below in Fig. 13.

It can be observed that even with the higher energy flux from GOES 16 received in the V band compared to that of the Rc band, the SNR of the V band data is still lower than the Rc band data as we predicted earlier with the objective function. This is due to the increase in the polluted sky background spectral radiance energy picked up by the telescope

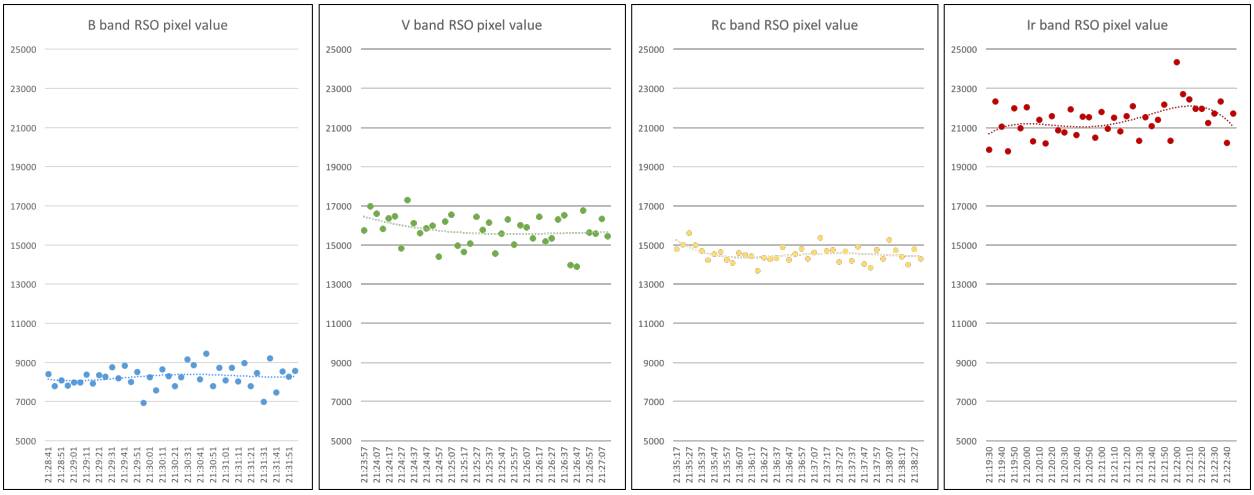

Fig. 12 GOES 16 energy flux, separated by the filter type applied, captured by the GT-SORT during the night of April 16^{th}.

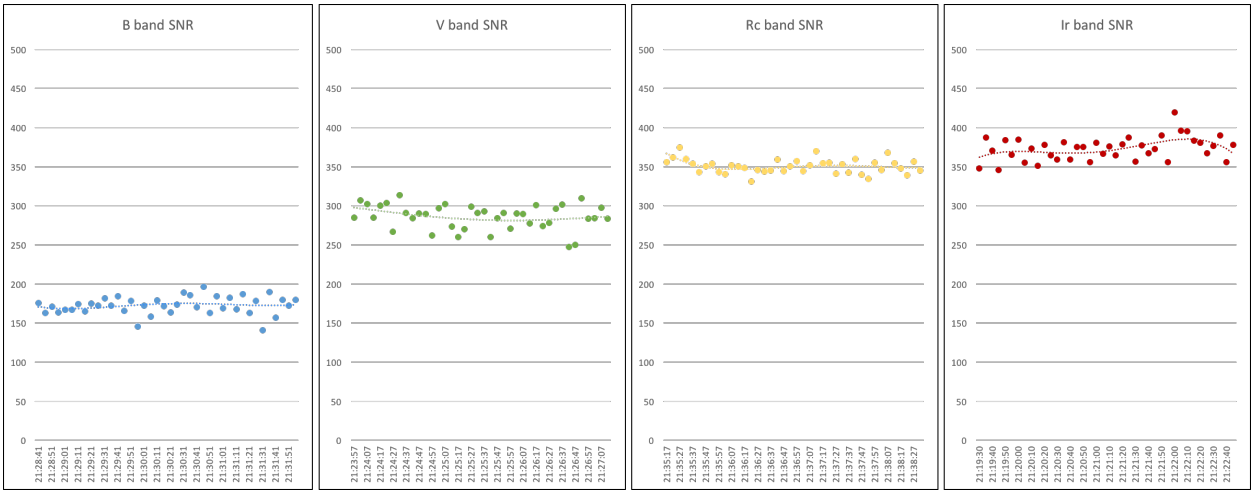

Fig. 13 GOES 16 SNR, separated by the filter type applied, captured by the GT-SORT during the night of April 16^{th}.

under the V band range from Fig. 4, which hinders the effectiveness of separating the target energy signature form the background energy. Whereas the Rc band data stands out more due to the lowered background pollution level. More importantly, the SNR result from this observation campaign agrees with the expectation generated with the objective function, where the Ir band data produced the highest SNR, closely followed by the Rc band data, then the V band, and finally the B band data with the lowest SNR.

V. Conclusion

In this paper, we explored the optimization of ground-based RSO detection tasks under light polluted environments. More specifically, we analyzed the wavelengths ranging from 400 nm to 900 nm to correspond to the operating range of

a typical CMOS sensor type CCD due to the previous work suggesting a overall optimal detection wavelength well into the infrared region, and the limited availability of a high resolution IR sensor to the general public. Of the four RSO material analyzed, it is determined that the optimal detection waveband should be in between the Rc and the Ir bands of the traditional Johnson Cousin's filter set.

An observation campaign was conducted on April 16^{th}, collecting experimental data of the GOES 16 GEO satellite with the Johnson Cousin's filter set applied. The results were presented with the resultant SNR of the target signal matching up to the the optimization results calculated with the objective function. This data supports the validity of the optimization model and suggests that an investment into a custom band-pass filter with a band-center located between the Rc band and the Ir band can be advantageous. This work also supports the previous effort of the general optimization of the SDA observing bands, suggesting that investments of SWIR sensors and custom infrared band-pass filters are warranted for more sophisticated operations.

Acknowledgments

This work was partially supported through an Internal Research and Development (IRAD) project from the Georgia Tech Research Institute.

References

[1] Badura, G., Valenta, C., Gunter, B., Renegar, L., and Wu, D., "Spectral Performance Optimization of Small Telescopes for Space Object Detection," *Proceedings of the <A href="https://www.amostech.com">Advanced Maui Optical and Space Surveillance Technologies Conference</A*, 2019, p. 27.

[2] Lambert, J. V., "Open-Filter Optical SSA Analysis Considerations," 2016.

[3] Coder, R. D., Jaunzemis, A. D., Mathew, M. V., Worthy, J. L., and Holzinger, M. J., "Georgia Tech Space Object Research Telescope," *Journal of Spacecraft and Rockets*, Vol. 54, No. 6, 2017, pp. 1399–1403. https://doi.org/10.2514/1.A33852, URL https://doi.org/10.2514/1.A33852.

[4] Lerner, K. L., and Lerner, B. W. (eds.), *Infrared Astronomy*, 5^{th} ed., chapter and pages, pp. 2353, 2356.

[5] Riker, J. F., and Butts, R. R., "The time-domain analysis simulation for advanced tracking (TASAT) approaches to compensated imaging," *Defense, Security, and Sensing*, 1992.

[6] Gibson, B., Jim, K., Cognion, R., and Pier, E. A., "Optical-Infrared Colors of GEO Satellites," *Advanced Maui Optical and Space Surveillance Technologies Conference*, 2013, p. E67.

[7] Djité, I., Magnan, P., Estribeau, M., Rolland, G., Petit, S., and Saint-pé, O., "Modeling and measurements of MTF and quantum efficiency in CCD and CMOS image sensors," *Sensors, Cameras, and Systems for Industrial/Scientific Applications XI*, Vol.

7536, edited by E. Bodegom and V. Nguyen, International Society for Optics and Photonics, SPIE, 2010, pp. 153 – 164. https://doi.org/10.1117/12.839175, URL https://doi.org/10.1117/12.839175.

[8] Budding, E., and Demircan, O., *Introduction to Astronomical Photometry*, Vol. 6, 2007.

[9] Fried, D. L., "Optical Resolution Through a Randomly Inhomogeneous Medium for Very Long and Very Short Exposures," *J. Opt. Soc. Am.*, Vol. 56, No. 10, 1966, pp. 1372–1379. https://doi.org/10.1364/JOSA.56.001372, URL http://www.osapublishing.org/abstract.cfm?URI=josa-56-10-1372.

[10] Schildknecht, T., "Optical astrometry of fast moving objects using CCD detectors." *Geod.-Geophys. Arb. Schweiz*, Vol. 49, 1994.

[11] Coder, R. D., and Holzinger, M. J., "Multi-Objective Design of Optical Systems for Space Situational Awareness," *Acta Astronautica*, Vol. 128, 2016, pp. 669–684. https://doi.org/http://dx.doi.org/10.1016/j.actaastro.2016.07.008.

[12] Coder, R., and Holzinger, M., "Sizing of a Raven-Class Telescope Using Performance Sensitivities," *Advanced Maui Optical and Space Surveillance Technologies Conference*, 2013, p. E28.

[13] Mamajek, E. E., Torres, G., Prsa, A., Harmanec, P., Asplund, M., Bennett, P. D., Capitaine, N., Christensen-Dalsgaard, J., Depagne, E., Folkner, W. M., Haberreiter, M., Hekker, S., Hilton, J. L., Kostov, V., Kurtz, D. W., Laskar, J., Mason, B. D., Milone, E. F., Montgomery, M. M., Richards, M. T., Schou, J., and Stewart, S. G., "IAU 2015 Resolution B2 on Recommended Zero Points for the Absolute and Apparent Bolometric Magnitude Scales," , 2015.

[14] Arora, J., "Introduction to Optimum Design," 1988.

[15] Hansen, M. P., and Malchow, D. S., "Overview of SWIR detectors, cameras, and applications," *Thermosense XXX*, Vol. 6939, edited by V. P. Vavilov and D. D. Burleigh, International Society for Optics and Photonics, SPIE, 2008, pp. 94 – 104. https://doi.org/10.1117/12.777776, URL https://doi.org/10.1117/12.777776.

[16] Suzhou ZWO CO., L., "ASI071 Manual," 2018. URL https://astronomy-imaging-camera.com/manuals/ASI071MC.

[17] Reyes, J., and Cone, D., "Characterization of Spacecraft Materials using Reflectance Spectroscopy," *The Advanced Maui Optical and Space Surveillance Technologies Conference*, 2018, p. 57.

[18] Lim, H., Young, J. L., Geisz, J. F., Friedman, D. J., Deutsch, T. G., and Yoon, J., "High performance III-V photoelectrodes for solar water splitting via synergistically tailored structure and stoichiometry," *Nature Communications*, Vol. 10, No. 1, 2019, p. 3388. https://doi.org/10.1038/s41467-019-11351-1, URL https://doi.org/10.1038/s41467-019-11351-1.

[19] Berk, A., Anderson, G. P., Bernstein, L. S., Acharya, P. K., Dothe, H., Matthew, M. W., Adler-Golden, S. M., Chetwynd, J. H., Richtsmeier, S. C., Pukall, B., Allred, C. L., Jeong, L. S., and Hoke, M. L., *MODTRAN4 radiative transfer modeling for atmospheric correction*, 1999, chapter and pages, pp. 348–353. https://doi.org/10.1117/12.366388.

[20] Quan, J., Zhang, Q., He, H., Liu, J., Huang, M., and Jin, H., "Analysis of the formation of fog and haze in North China Plain (NCP)," *Atmospheric Chemistry and Physics*, Vol. 11, No. 15, 2011, pp. 8205–8214. https://doi.org/10.5194/acp-11-8205-2011, URL https://www.atmos-chem-phys.net/11/8205/2011/.

[21] Vautard, R., Yiou, P., and van Oldenborgh, G. J., "Decline of fog, mist and haze in Europe over the past 30years," *Nature Geoscience*, Vol. 2, No. 2, 2009, pp. 115–119. https://doi.org/10.1038/ngeo414, URL https://doi.org/10.1038/ngeo414.

[22] Shirkey, R. C. A. R. L. W. S. M. R. N., "Sky Glow from Cities: The Army Illumination Model v2," *Defense Technical Information Center*, 2011. URL https://apps.dtic.mil/dtic/tr/fulltext/u2/a553794.pdf.

[23] Goodman, S. J., "Chapter 1 - GOES-R Series Introduction," *The GOES-R Series*, edited by S. J. Goodman, T. J. Schmit, J. Daniels, and R. J. Redmon, Elsevier, 2020, pp. 1 – 3. https://doi.org/10.1016/B978-0-12-814327-8.00001-9, URL http://www.sciencedirect.com/science/article/pii/B9780128143278000019.

[24] A, C. P.-. R., "GOES-R Series DataBook," 2019.

[25] Spectrobal Inc, C. . U., 12500 Gladstone Avenue Sylmar, "28.3% Ultra Triple Junction (UTJ) Solar Cells," 2008. URL http://www.spectrolab.com/DataSheets/TNJCell/utj3.pdf.

[26] "The Photometry Primer," *A Practical Guide to Lightcurve Photometry and Analysis*, Springer New York, New York, NY, 2006, pp. 27–46. https://doi.org/10.1007/0-387-33391-6_4, URL https://doi.org/10.1007/0-387-33391-6_4.

[27] Merline, W. J., and Howell, S. B., "A realistic model for point-sources imaged on array detectors: The model and initial results," *Experimental Astronomy*, Vol. 6, No. 1, 1995, pp. 163–210. https://doi.org/10.1007/BF00421131, URL https://doi.org/10.1007/BF00421131.